JACS
JOURNAL OF THE AMERICAN CHEMICAL SOCIETY

ARTICLE

pubs.acs.org/JACS

Combinatorial Atmospheric Pressure Chemical Vapor Deposition (cAPCVD): A Route to Functional Property Optimization

Andreas Kafizas and Ivan P. Parkin*

Materials Chemistry Research Centre, Department of Chemistry, University College London, 20 Gordon Street, London, U.K. WC1H 0AJ

Supporting Information

ABSTRACT: We demonstrate how combinatorial atmospheric pressure chemical vapor deposition (cAPCVD) can be used as a synthetic tool for rapidly optimizing the functional properties of thin-films, by analyzing the self-cleaning properties of tungsten doped anatase as an example. By introducing reagents at separate points inside the reactor, a tungsten/titanium compositional gradient was formed and a diverse range of film growth conditions were obtained. By partially mixing the metal sources, a combinatorial film with a compositional profile that varied primarily in the lateral plane was synthesized. A combinatorial thin-film of anatase TiO_2 doped with an array of tungsten levels as a solid solution ranging from 0.38−13.8 W/Ti atom % was formed on a single glass substrate. The compositional−functional relationships were understood through comprehensively analyzing combinatorial phase space, with 200 positions investigated by high-throughput methods in this study. Physical and functional properties, and their compositional dependencies, were intercorrelated. It was found that increases in photocatalytic activity and conductivity were most highly dependent on film crystallinity within the 0.38−13.8 atom % W/Ti doping regime. However, enhancements in photoinduced surface wetting were primarily dependent on increases in preferred growth in the (211) crystal plane.

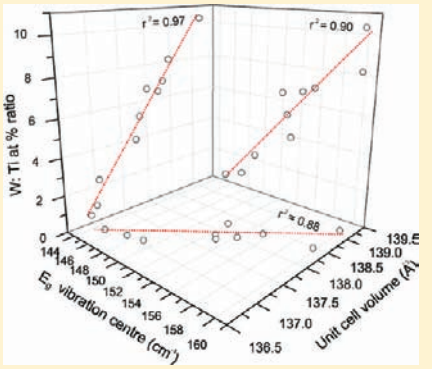

Thin-films of anatase titanium dioxide (TiO_2) have been extensively studied due to their multifunctional applications in self-cleaning,[1,2] water-splitting,[3−5] and gas-sensing devices.[6] The majority of research has focused on improving the self-cleaning properties of thin-films through doping or composite formation.[7−11] In addition, there has been some recent interest in improving the material's conductivity through transition metal ion doping for optoelectronic applications.[12−14]

The most common method of forming TiO_2 thin-films is through the preparation and coating of a sol−gel solution, and when attempting to optimize composition for a particular function, a series of these films with varying composition would be required.[15] However, atmospheric pressure chemical vapor deposition (APCVD) has been used to rapidly produce TiO_2 thin-films of equivalent quality and uniformity on the minute time-scale.[16] More importantly, TiO_2 thin-films with significant variations in phase, thickness, and dopant level have also been achieved using combinatorial atmospheric pressure chemical vapor deposition (cAPCVD).[17−21] Where traditional APCVD methods allow reagent gaseous precursors to become homogenously mixed before entering the reactor, cAPCVD implements separate points of entry.[22] The gradient in gas mixtures across the reactor induces compositional film growth, producing a single film with such a variety of makeup that distinctly different functional properties can be found at different points along the film. cAPCVD is a relatively new synthetic method that has been used to decipher the relationship between composition and the material's functional properties in a number of systems.[17−21,23] One combinatorial system showed a transitional change in phase from the recently discovered $Ti_{3-\delta}O_4N$ ($0.06 < \delta < 0.25$) pseudobrookite phase[24] to anatase TiO_2.[18] A simultaneous assessment of the photocatalysis showed that pure pseudobrookite was a more active photocatalyst under UVA lighting conditions than either pure anatase or phase mixtures. More recently, another combinatorial system composed of anatase TiO_2 with varying levels of substitutional and/or interstitial nitrogen doping was investigated.[20] By spraying an "intelligent ink" evenly over the film, the photocatalytic response through changes in the ink's color was simply monitored through digital photography[25,26] and indicated that doping nitrogen purely in interstitial sites over substitutional sites yielded a more effective photocatalyst. The convenience of having such a variety of unique compositions over a single film is 2-fold. First, only one synthesis is required and can be achieved using a cAPCVD process, and second, positions can be rapidly characterized, ideally by preprogrammed machinery with X−Y maneuverable stages or by simultaneous assessment.

Incorporating tungsten within anatase TiO_2 has increased the conductivity,[27,28] gas-sensing,[29] photoinduced surface wetting,[30] and photocatalytic properties[9,31,32] of the material. In an effort to optimize the self-cleaning properties, we present the cAPCVD

Received: September 13, 2011
Published: November 04, 2011

synthesis of an anatase TiO_2 thin-film with varying levels of tungsten dopant. Through a number of analysis methods we demonstrate how the physical and functional properties of this material inter-relate. A strong inter-relationship between the unit cell volume, level of tungsten doping, and shift of the primary Raman active E_g vibrational mode was revealed. It was also found that the photocatalysis and conductivity properties were most highly dependent on film-crystallinity, whereas the property of photoinduced wetting was most highly dependent on changes in preferred growth in the 211 plane.

EXPERIMENTAL SECTION

Combinatorial Deposition. All chemicals used in this study were purchased from Sigma-Aldrich Chemical Co; glycerol 99.5%, hydroxy ethyl cellulose [average $M_v \approx 90{,}000$], ethyl acetate 99%, methanol 99%, resazurin 92%, stearic acid 99%, titanium(IV) chloride 99.9%, tungsten(VI) chloride 99.9%. Nitrogen (oxygen free) gas-cylinders were supplied by BOC. The glass-substrate, consisting of a standard piece of 3.2 mm thick float glass coated with a 50 nm SiO_2 barrier layer, was supplied by Pilkington NSG Group.

A combinatorial thin-film comprised solely of the anatase TiO_2 phase with varying levels of tungsten solid solution doping from 0.38 to 13.8 atom % W/Ti ratio was synthesized using cAPCVD. The film was deposited onto a standard float glass slide of dimensions 90 mm × 225 mm × 3.2 mm (length × breadth × thickness) inside a cold-walled reactor heated on its underside through a graphite block. The substrate contained a silica barrier layer (≈50 nm thick) that prevented migration of ions within the glass into the thin-film. A schematic of the apparatus used is shown in Figure 1.

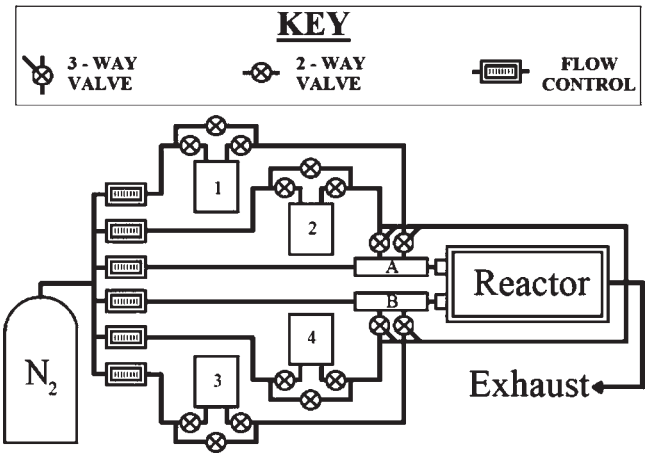

Figure 1. Schematic of the cAPCVD apparatus used in the synthesis of an anatase TiO_2 film with graded levels of tungsten doping.

The reagents were volatilized in heated bubblers, transported to their respective mixing chamber (A/B), and pushed with a plain line through the baffle manifold and into the reactor by an inert nitrogen carrier gas. The tungsten and titanium sources were introduced into the baffle at opposite sides, with WCl_6 and $TiCl_4$ transported from bubblers 1 and 3, respectively. Ethyl acetate (oxygen source) was introduced into the baffle at both sides, being carried from bubblers 2 and 4. The baffle was designed to allow a partial lateral mixing of the gases before entering the reactor, creating a horizontal gradient in the W/Ti ratio in the precursor mix and a range of deposition conditions, instigating the conditions for the combinatorial aspect of this work. The parameters used to deposit the combinatorial film in this study are shown in Table 1. The carbon heating block was maintained at 525 °C during the 60 s deposition. Mass flow rates (mol min^{-1}) from vapor pressure (mm Hg) curves yielded reagent molar ratios (normalized to $TiCl_4$).

Analytical Methods. A map labeled with a "battleship" style coordinate system was used to locate and analyze 200 distinct positions over the film. The characterization method and corresponding positions analyzed are specified in Figure 2, which shows a picture of the combinatorial film overlaid by this reference system.

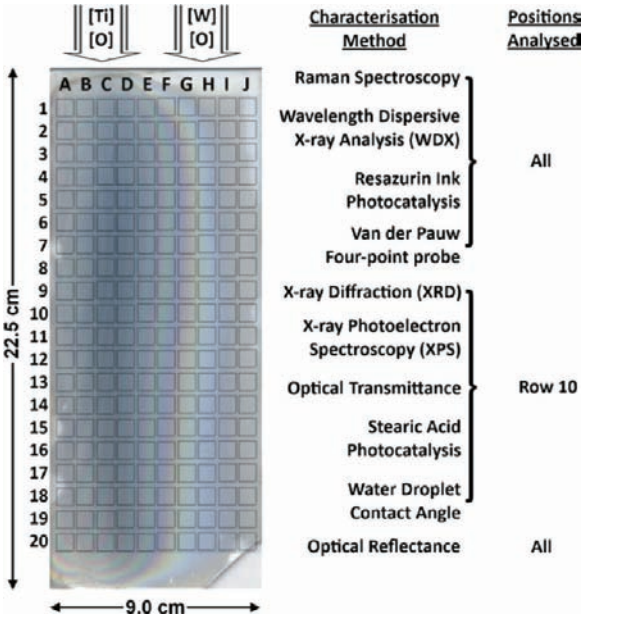

Figure 2. Picture of the combinatorial film and superimposed grid reference system where neighboring grid positions are spaced ≈0.75 cm apart. The characterization method and positions analyzed are stated adjacently. The relative positions of the gas inlets where each metal and oxygen source entered the reactor are also shown.

Table 1. Reaction Conditions in the cAPCVD Synthesis of an Anatase TiO_2 Thin-Film with Graded Levels of Tungsten Doping

	mixing chambers		bubblers			
			1	2	3	4
	A	B	WCl_6	MeCOOEt	$TiCl_4$	MeCOOEt
temp (°C)	254	246	281	45.0	66.0	37.0
flow rate (L/min)	1.0	4.0	4.0	0.20	1.2	0.25
vapor pressure (mm Hg)			191	233	83	166
flow (10^{-3} mol min^{-1})			55	3.6	6.0	2.9
molar ratios			9.2	0.6	1.0	0.5

dx.doi.org/10.1021/ja208633g |J. Am. Chem. Soc. 2011, 133, 20458–20467

Physical Properties. Wavelength dispersive X-ray (WDX) analysis was performed on a Philips ESEM. The W/Ti atom % composition was derived from the Ti Kα-line (4508 eV) and W Lα-line (8376 eV) emission intensities. X-ray photoelectron spectroscopy (XPS) was performed at Cardiff University using a Kratos Axis Ultra-DLD photoelectron spectrometer with a monochromatic Al Kα source. High resolution scans were recorded for the principal peaks of W(4f)/Ti(3d), W(4d), Ti(2p), O(1s), C(1s), Cl(2p), and Si(2p) at a pass energy of 40 eV. The peaks were modeled using CasaXPS software[33] with the binding energies adjusted to adventitious carbon (284.5 eV).[34] Raman spectroscopy was performed using a Renishaw 1000 spectrometer equipped with a 632.8 nm laser. Positions were analyzed over the 100−800 cm^{-1} range. X-ray diffraction (XRD) was conducted using a microfocus Bruker GADDS powder X-ray diffractometer with a monochromated Cu Kα (1.5406 Å) source. The optical reflectance and transmittance spectra were recorded over the 300−2500 nm range using a Helios double beam instrument. Atomic force microscopy (AFM) was conducted on a Veeco Dimension 3100 in air using a silicon tipped cantilever over 1 μm^2 and 100 μm^2 sample areas.

Functional Properties. Water droplet contact angles were measured using a First Ten Angstroms 1000 device[35] with a side mounted rapid-fire camera after casting an 8.6 μL droplet from a fixed height onto the surface. The droplets were cast at set times between UVC irradiations (254 nm: Vilber Lourmat 2 × 8W). Before assessing the photocatalysis, samples were first washed with distilled water, rinsed with isopropanol, and irradiated for 1 h with UVC light to clean and activate the surface. The photocatalysis test involved spraying a resazurin ink, formulated as originally prepared by Mills et al.,[36] evenly over the surface of the film.[25] The photocatalytic reduction reaction was induced by UVA light (365 nm: Vilber Lourmat 2 × 8W) and monitored by taking digital images (Epson Perfection 1200 Photo Scanner—200 ppi) of the film and the degrading ink layer at time intervals. The changes in digital color at each grid position were extracted using custom-made software.[37] The stearic acid photocatalysis test was conducted at point positions. A stearic acid overlayer was formed by casting droplets from a 0.02 M methanolic solution. Any traces of methanol were first removed by oven drying samples for 1 h at 50 °C. The reaction was instigated and propagated by irradiating samples with UVC light. Infrared spectroscopy, performed using a Perkin-Elmer RX-I instrument, was carried out to measure the decrease in stearic acid C−H bond absorbances over the 2980−2800 cm^{-1} range. A fixed-width in-line spring-mounted four-point electrode was set up in house for measuring sheet resistance by the van der Pauw method.[38] A constant voltage was applied through grid-positions along the material using a Maplin N93CX switching mode power supply. Voltages and currents were measured using Caltek CM2700 and Sinometer M-830B meter diodes, respectively.

RESULTS AND DISCUSSION

Physical Characteristics. An anatase TiO_2 thin-film with a gradient in the W doping level (0.38−13.8 W/Ti atom %) was grown by cAPCVD. The synthesis involved the combination of $TiCl_4$ and WCl_6 metal sources with an ethyl acetate oxygen source at 525 °C, coating the entire glass substrate. Color bands due to variations in the thickness of the coating were observed, characteristic of thin-films with high refractive indices. The color contours alternated chiefly from green to purple and maximized toward the middle-left section: the thickest area of the film. A blue tinge, observed best off-angle, was also seen, characteristic of tungsten doped solid solutions.[22]

Combinatorial Characteristics. *Wavelength Dispersive X-ray Mapping.* The tungsten incorporated was determined by wavelength dispersive X-ray (WDX) analysis for all 200 of the allotted grid positions. A 3-dimensional bar chart of the W/Ti ratio (atom %) is shown in Figure 3. A substantial variation in the tungsten dopant level was observed, ranging from 0.38 to 13.8 W/Ti atom %. Interestingly, an almost linear increase in dopant level was seen in rows upon movement from A to J. However, very little change in the W doping level was observed along the columns. This indicated that precursor flows were laminar and that lateral diffusion was largely nonexistent.

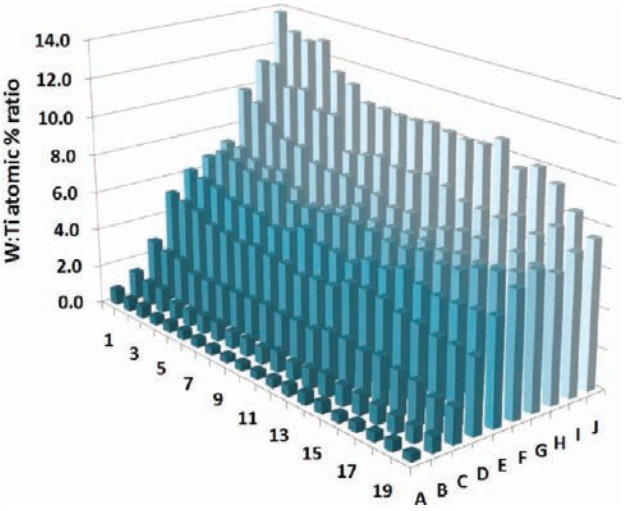

Figure 3. 3-dimensional bar chart of the W/Ti ratio (atom %) at each of the 200 grid positions across the thin-film. Values were determined from WDX analysis of the Ti Kα and W L_α emission lines.

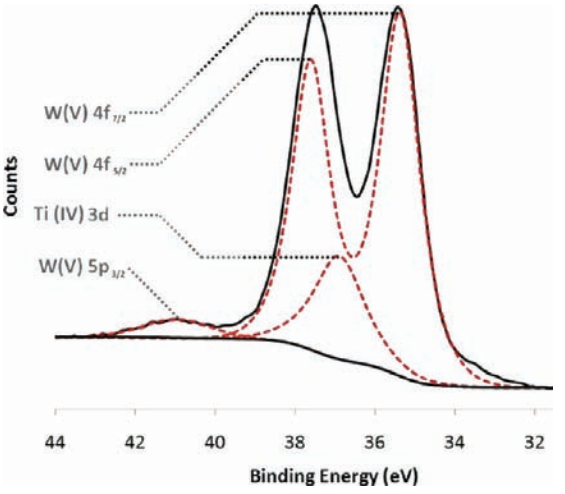

Figure 4. X-ray photoelectron spectral profile at grid position J10 of the W 4f/Ti 3d binding energy region; deconvoluted portions shown in dotted red lines.

X-ray Photoelectron Spectroscopy Mapping. Each position along row 10 was investigated by X-ray photoelectron spectroscopy (XPS). The binding energies of the prominent Ti $2p_{3/2}$ excitation varied very little across the row, ranging from 458.2 to 458.5 eV, and were attributed to the presence of Ti^{4+}.[39] The most intense peaks in the XPS spectrum of tungsten are due to electronic excitations from the W 4f orbital; however, these fall in the same region as the Ti 3d excitations (Figure 4).[28] Therefore, both the W 4f and the W 4d regions were analyzed to discern the surface dopant level and composition. The binding

Table 2. Physical−Functional Property Data from Row 10 in the cAPCVD Produced Anatase TiO_2 Thin-Film with Graded W Doping[a]

		A10	B10	C10	D10	E10	F10	G10	H10	I10	J10
					Physical Properties						
WDX (±1%)	W/Ti ratio (atom %)	0.42	0.87	2.27	3.93	5.20	6.40	6.65	6.95	8.13	10.3
XPS (±15%)		2.05	1.88	2.18	2.13	2.20	2.47	3.78	5.41	13.5	28.8
Raman	principle E_g mode (cm^{-1} ± 0.1%)	144.9	147.1	148.8	153.0	152.5	151.9	154.1	155.3	159.7	159.8
XRD	volume ($Å^3$ ± 0.1%)	136.9	137.0	137.1	137.8	137.9	138.2	138.0	138.3	138.5	139.2
	crystallite size (nm ±1%)	19.5	19.9	18.7	18.7	18.1	17.3	16.9	16.3	16.4	14.2
reflectance	thickness (nm ±1%)	940	980	820	590	370	210	120	70	<70	<70
AFM	root mean squared (nm ± 0.1%)	11.1	10.6	8.7	6.9	4.9	3.2	3.3	2.8	2.6	2.5
					Functional Properties						
transmittance	bandgap (eV ± 1%)	3.13	3.16	3.18	3.23	3.26	3.30	3.28	3.29	3.30	3.32
resistance	2-point (10^4 Ω ± 10%)	4.00	2.89	4.96	9.50	19.5	38.3	86.3	312	1390	BD
	4-point (10^4 Ω/□ ± 10%)	2.05	1.94	2.61	4.74	10.1	17.3	35	78.3	BD	BD
	ρ (10^{-2} Ωm ± 10%)	1.92	1.90	2.14	2.80	3.73	3.64	4.20	6.66	BD	BD
photocatalysis	stearic acid (10^{-5} FQE ± 5%)	5.21	4.95	3.75	2.55	2.53	2.48	1.22	1.14	1.93	0.99
	resazurin (10^{12} $cm^{-2}s^{-1}$ ± 10%)	2.36	2.62	2.36	2.03	1.46	1.03	0.78	0.64	0.49	0.40
	resazurin (10^{-4} FQE ± 10%)	5.04	5.58	5.04	4.34	3.13	2.20	1.66	1.36	1.04	0.85
	resazurin (10^{-4} FQY ± 10%)	8.46	10.6	9.83	9.28	8.27	7.47	5.90	4.61	5.08	2.58
water contact angle	pre-UV (° ± 10%)	71	73	76	70	70	72	67	70	73	69
	post-UV minimum (° ± 10%)	4.6	7.9	5.4	8.0	8.2	6.0	10	16	16	18

[a] BD = beyond detection limits of the apparatus.

energy of the deconvoluted W 4f and W 4d excitations did not vary significantly across the row, ranging from 35.2 to 35.7 eV in W $4f_{7/2}$ peaks and from 246.6 to 247.6 eV in W $4d_{5/2}$ peaks. This indicated that tungsten was primarily present in a single oxidation environment. The average binding energy attributed to these tungsten $4f_{7/2}$ states varies from W^{4+} = 33.1 eV to W^{5+} = 35.0 eV to W^{6+} = 36.4 eV.[28,32,40−45] The average $4f_{7/2}$ binding energy seen across the combinatorial film was 35.4 eV, indicating that the tungsten dopant was predominantly in the W^{5+} state, where some unresolvable levels may have existed as W^{6+}. The W/Ti ratio (atom %) was from the average of both W 4f and W 4d environments (Table 2). The relative tungsten doping level from WDX and XPS analyses can be related to the bulk and surface tungsten doping levels, respectively. Although the average bulk and surface levels of tungsten doping were approximately equal across the row, where the W/Ti ratio = 5.1 atom % from WDX analysis and 6.4 atom % from XPS analysis, there was no proportional relationship between the levels of bulk and surface doping (Table 2). In fact, tungsten doping levels increased exponentially at the surface and more linearly in the bulk on going from positions A10 to J10. This was attributed to surface segregation effects that were most pronounced at positions I10 and J10.

Raman and X-ray Diffraction Mapping. All Raman patterns acquired over the 200 allotted grid positions showed peaks consistent with that of anatase TiO_2 tetragonal symmetry.[46] The width of the Raman peaks increased systematically across the film, where the widest peaks were seen in the regions of highest tungsten doping. The width of a Raman peak is directly related to film-crystallinity, where increasingly wider peaks correspond to an increasingly amorphous film.[47] In addition, an increase in the blue-shift in the principle E_g vibrational mode of anatase TiO_2[46] was observed with increased tungsten doping. Such an effect is common, where increased solid solution doping restricts phonons and increases the energy for a vibrational excitation to occur.[48,49] A systematic decrease in peak intensity coupled with an increasing blue-shift in the principle E_g mode was seen on moving from position A10 to J10. Each peak was individually fit to a Gaussian model, allowing precise values for the peak centers and degree of blue-shift to be determined (Table 2). A consistent increase in the excitation energy of the principle E_g mode was observed with tungsten content. A strongly correlating linear relationship between the level of tungsten doping and degree of blue-shift in the principle E_g mode was observed (r^2 = 0.90), where a low doping level of W/Ti = 0.42 atom % at position A10 caused a marginal shift to 144.9 cm^{-1} and a high doping level of W/Ti = 10.3 atom % at position J10 caused a more substantial shift to 159.8 cm^{-1}. Kim et al. noted from the analysis of a series of tungsten doped nanocrystals that there was a regular shift in the E_g band from 144.3 to 149.3 cm^{-1} over 0−20 atom % W/Ti.[49] A less pronounced shift in the E_g mode was observed in Kim et al.'s study, as their materials contained significant levels of W^{6+} ion doping, which disrupted the lattice less so than the larger W^{5+} ion.

X-ray diffraction was employed to quantify the level of lattice strain suggested from the blue-shifts in Raman patterns. Positions along row 10 were studied for a direct comparison (Figure 5). The patterns confirmed the presence of single phase anatase TiO_2 ($I4_1/amdz$, a = 3.785 Å, c = 9.512 Å). No evidence of a separate tungsten oxide phase was seen, also confirming the formation of a solid solution. A drop in the intensity of patterns was attributed to both a thinner and less crystalline film. The film-crystallinity was quantified by applying the Scherrer equation to the prominent (101) diffraction peak.[50] A decrease in average crystallite size from 19.9 nm at position A10 to 14.2 nm at position J10 was seen. A closer look at the (101) diffraction peaks revealed a trend, where peaks systematically shifted to lower

dx.doi.org/10.1021/ja208633g |J. Am. Chem. Soc. 2011, 133, 20458–20467

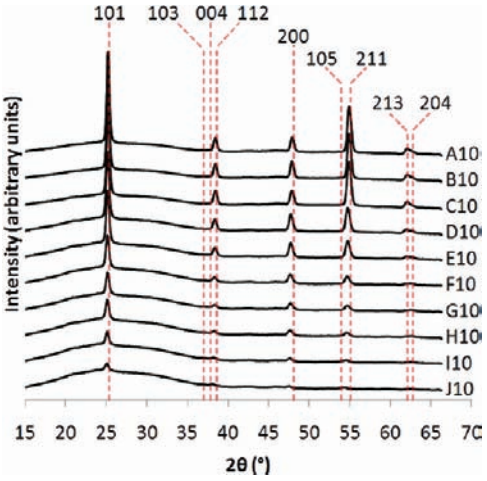

Figure 5. Stacked X-ray diffraction patterns of the positions analyzed across row 10.

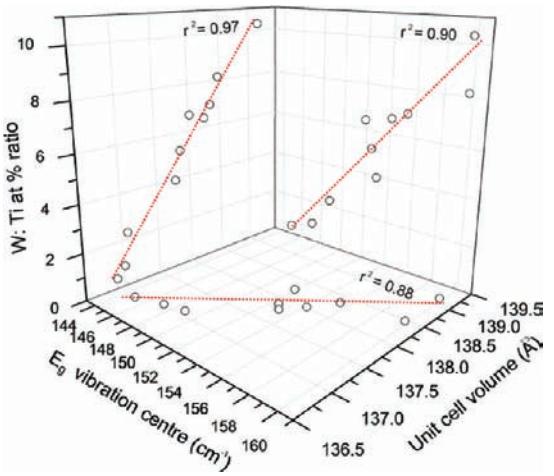

Figure 6. 3-dimensional plot of the strong inter-relationships between the blue-shift of the principle Raman active E_g mode (cm^{-1}), unit cell expansion ($Å^3$), and tungsten doping level (W/Ti ratio atom %) for the positions analyzed across row 10.

angles from position A10 to J10. In fitting the full diffraction pattern to a Le Bail refined model,[51] a lattice expansion was evident, with the unit cell volume increasing across the row from 136.9 $Å^3$ at position A10 to 139.2 $Å^3$ at position J10. The most significant increases were seen in the a/b direction. A strong linear correlation between the level of tungsten doping and the unit cell volume was observed ($r^2 = 0.97$). It therefore became evident that the three physical properties (i) tungsten doping level, (ii) blue-shift of the principle Raman E_g mode, and (iii) lattice expansion were inter-related, as shown in Figure 6.

The inter-relationship comprehensively quantified what one would expect from doping anatase TiO_2 with a larger cation. As increasing levels of tungsten were inserted within the TiO_2 matrix, the strain on the unit cell increased and pushed the surrounding atoms further apart. This in turn constricted phonons and increases the energy required to cause the principle Raman E_g excitation. It is also worthy of note that the most significant increases in unit cell occurred across the a/b lattice plane, the direction in which the E_g vibrational mode operates.[46] This physical inter-relationship is quite useful if one wants to quickly estimate the W/Ti doping level in W-doped anatase TiO_2 materials by either Raman spectroscopy or X-ray diffraction. A quick estimate would come from finding the exact location of the principle E_g mode (cm^{-1}) through Raman spectroscopy:

$$\text{W/Ti doping level (atom \%)} = 0.624E_g - 89.9 \quad (1)$$

Nevertheless, as the degree of correlation observed in determining this relationship from our studies ($r^2 = 0.90$) was lower than the degree of correlation observed between the unit cell volume and the level of tungsten doping ($r^2 = 0.97$), there would be greater accuracy in predicting the level of tungsten doping from X-ray diffraction experiments:

$$\text{W/Ti doping level (atom \%)} = 4.347V - 594.3 \quad (2)$$

where V is the unit cell volume in $Å^3$. These lattice expansions corresponded to average ionic radii of 0.61 Å and 0.55 Å for W^{5+} and Ti^{4+}, respectively. As there is no direct study, to our knowledge, on the lattice expansion of W-doped TiO_2 solid solutions, these values could only be compared with averages from the literature. The ionic radius of W^{5+} compared well (0.62 Å);[52] however, the ionic radius of Ti^{4+} was slightly lower than what was normally observed (0.60 Å).[53]

Film Thickness Mapping. The combinatorial film showed a number of color bands due to changes in film thickness (Figure 2). Such color bands are observed in anatase TiO_2 thin-films (ranging from ≈0.1−1 μm in thickness) due to optical interference.[20] This effect gives rise to the differing colors seen in anatase thin-films at differing film thicknesses. Transmittance spectra unveil several maxima and minima at specific wavelengths that depend entirely on the thickness and refractive index of the film. This enables the thickness of the medium to be determined using the Swanepoel method.[54] Figure 7a shows the exact locations in which the reflectance spectra were measured and the corresponding wave-patterns. By assuming growth between color bands was linear, the thickness at each boundary was derived through weighted averages. Applying this assumption further, the thickness at each grid position could also be found. A thickness contour map was constructed, as shown in Figure 7b. Film-thicknesses could not be determined for grid positions stationed in columns I and J, as the film was too thin to show any interference bands over the region analyzed (200−2500 nm). However, observed thicknesses ranged from as low as 70 nm (position H10) to as high as 810 nm (position B10).

Surface Topography Mapping. Atomic force microscopy was employed to map the surface topography and roughness of films across row 10. Topographical images are provided in the Supporting Information (S1). At position A10, long "wormlike" grains were observed. Moving across the row, from position A10 along to J10, the surface structure gradually changed, becoming grainier in nature. This coincided with a systematic decrease in surface roughness, where the root mean squared roughness decreased from 11.1 nm at position A10 to 2.52 nm at position J10.

Combinatorial Reaction Chemistry. It has been suggested that the APCVD reaction of $TiCl_4$ and H_2O precursors has a lower activation energy than the APCVD reaction of $TiCl_4$ and ethyl acetate;[55] however, CVD thin-films formed from $TiCl_4$ and H_2O are notoriously blotchy and have a tendency to flake. This is due to the greater propensity for the reaction of $TiCl_4$ and H_2O to proceed in the gas phase rather than at the surface of the

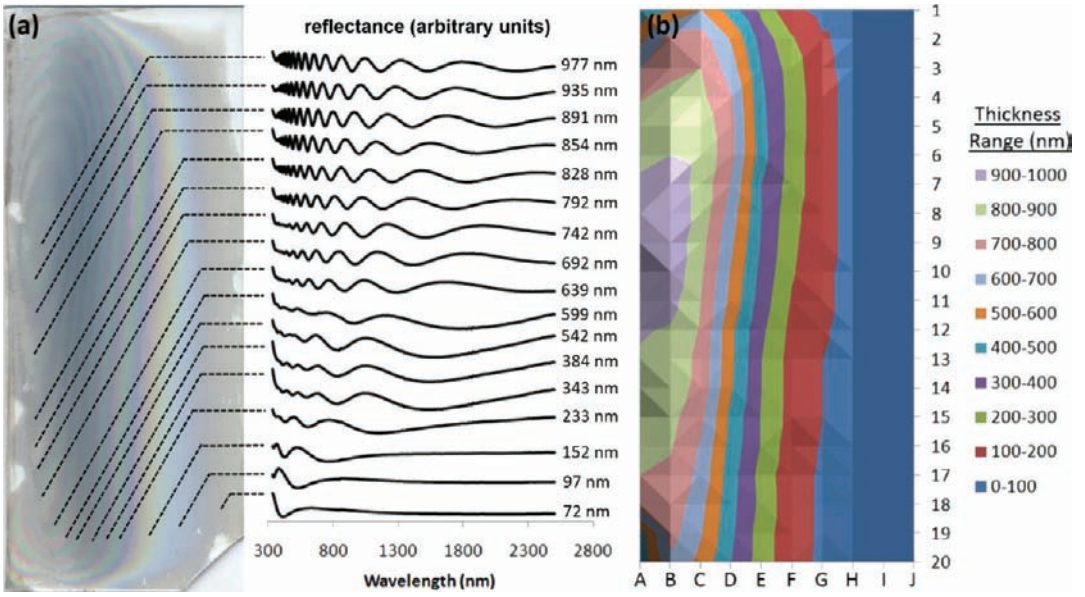

Figure 7. (a) Map displaying the position at which each interference color band was analyzed by reflectance spectroscopy alongside its corresponding reflectance wave-pattern and Swanepoel derived film-thickness and (b) color contour map of film-thickness for the 200 allotted grid positions across the combinatorial film determined by approximating the linear growth between interference fringes.

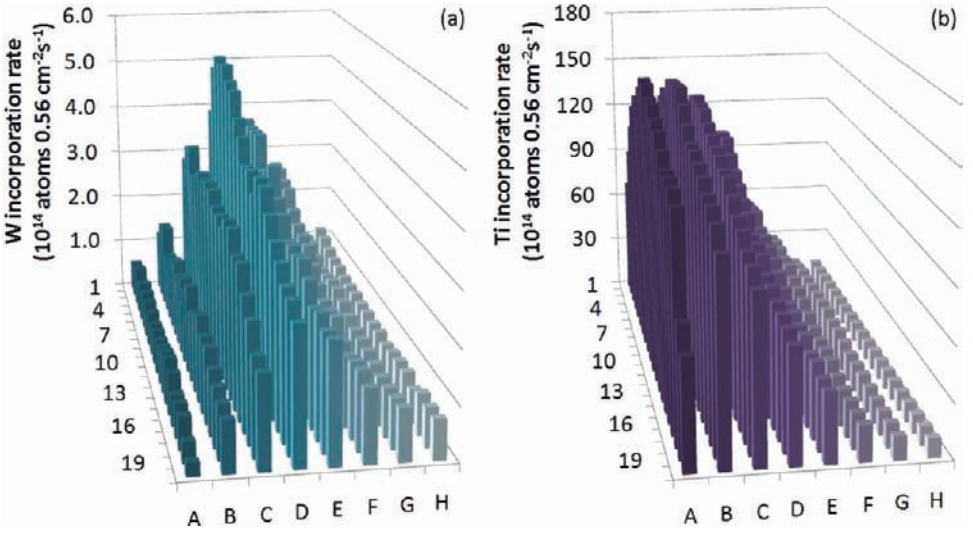

Figure 8. 3-dimensional bar charts showing the reaction rates (10^{16} molecules/min) of (a) WCl_6 and (b) $TiCl_4$ across the combinatorial film formed by the cAPCVD of $TiCl_4/WCl_6$ and ethyl acetate at 525 °C. Columns I and J were omitted, as the film was too thin.

substrate. The exact mechanism by which $TiCl_4$ reacts with ethyl acetate to form TiO_2 thin-films by APCVD is not known.[55] However, it has been suggested that ethyl acetate decomposes at the surface to produce oxidant species such as ethanol (eq 3a), which in turn dehydrates to evolve water and ethane (eq 3b). With water present, the surface reaction could proceed by a simple hydrolysis reaction with $TiCl_4$ (eq 3c):

$$CH_3COOC_2H_5 \rightarrow CH_3CH_2OH + C_2H_2O \quad (3a)$$

$$CH_3CH_2OH \rightarrow H_2O + C_2H_4 \quad (3b)$$

$$H_2O + TiCl_4 \rightarrow TiO_2 + 4HCl \quad (3c)$$

Given the similar chemistry of metal chlorides, we propose that WCl_6 incorporated in the same way.

The ethyl acetate oxygen source was the limiting reagent in this reaction. This was fundamental to the quality of the films produced, as higher levels of ethyl acetate can cause carbon contamination.[17] As the ethyl acetate precursor entered the reactor from both sides in approximately equal molar ratio, the precursor was uniformly distributed across the substrate, making a direct comparison of the incorporation rates of the Ti and W metal sources fair. Through mapping the metal ratio incorporated across the combinatorial film (Figure 3) as well as film thickness (Figure 7), we were able to calculate the incorporation rate of each metal source at each grid square (except for columns I and J, where the film thickness was not attained), shown as 3-dimensional bar charts in Figure 8.

Strong carrier gas flow rates were used for the combinatorial deposition. A total of 5.20 L min^{-1} entered the reactor *via* mixing chamber A carrying the WCl_6 source, and on the opposite side, a total of 5.45 L min^{-1} entered *via* mixing chamber B carrying the $TiCl_4$ source. Given the small volume inside the reactor (≈0.25 L), these gas flows would have passed through the reactor in as little as 1 s. The growth profile, with bands of film thickness running parallel to each other and in the direction of gas flow, indicated that there is virtually no lateral diffusion of the metal precursors once inside the reactor. In this system, the metal precursors were partially mixed inside the baffle manifold.

The film showed no pinhole defects, and no particulates were seen exiting the exhaust, indicating that the reaction was predominantly surface based. From mapping film-thickness, anatase TiO_2 film growth was observed to be most rapid in the middle left section of the film. A large disparity in film-thickness was observed across the combinatorial film. For example, at least a factor of 10 difference in thickness was observed upon moving from position A10 (940 nm) to J10 (<70 nm). This was attributed to the lateral diffusion barrier in the movement of the $TiCl_4$ source. From assessing the trends in incorporation rate (Figure 8), the reaction of $TiCl_4$ was observed to be surface reaction rate limited and not mass transport limited for columns C−J. However, in columns A−C, the concentration of the level of Ti incorporated decreased from rows 12 to 20, indicating that the reaction is in part more mass-transport limited. A similar effect was observed for WCl_6, where the rate of reaction marginally decreased down the columns.

During this deposition, the mass flow of WCl_6 was almost ten times larger than that of $TiCl_4$ (Table 2). Quite the contrary to this, anatase TiO_2 formed the main structure with just 5.3 atom % tungsten doping on average. It was clear that the reactivity of $TiCl_4$ was far superior to that of WCl_6 under the conditions imposed. The average incorporation rate of Ti corresponded to 1.21×10^{16} atoms 0.56 cm^{-2} s^{-1} (0.56 cm^2 = area of each grid square, Figure 2) and was more than 30 times greater than the average incorporation rate of W (3.3×10^{14} molecules 0.56 cm^{-2} s^{-1}). With these respective incorporation rates and molar ratios in mind, the $TiCl_4$ source would have reacted *ca.* 335 times more rapidly than the WCl_6 source.

Functional Characteristics. *Bandgap Mapping.* Transmittance spectroscopy showed a gradual blue-shift in the band edge from position A10 to J10. The bandgap was subsequently determined for each position through extrapolating Tauc plots of transmittance data.[56] The bandgap energy increased quite steadily from 3.13 eV at position A10 to 3.32 eV at positions J10. Two phenomena could cause such an effect: (i) the Moss−Burstein effect[57] or (ii) decreasing crystallinity. Across row 10, both the concentration of n-type dopants (W-doping level) as well as the degree of amorphousness increased, making both explanations feasible. In order to determine which effect was playing the more dominant role, both the bulk tungsten doping level (WDX analysis) and average crystallite size (XRD analysis) were plotted against the bandgap energy. A stronger relationship was observed between the bulk tungsten doping level and the bandgap energy (r^2 = 0.94) rather than the average crystallite size (r^2 = 0.79). This indicated that the Moss−Burstein effect was the primary cause for the bandgap increase across the material. This result was contrary to what was proposed by Takeuchi et al., where the introduction of W-dopants within a solid-solution in anatase TiO_2 formed shallow states in the valence band that trapped charge carriers.[27]

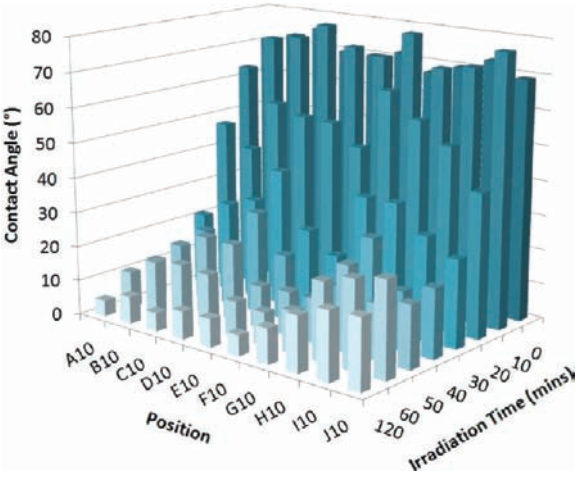

Figure 9. 3-dimensional bar chart stack of water droplet contact angle with cumulative UVC irradiation time along row 10.

Photoinduced Wettability Mapping. The water droplet contact angle was measured for positions across row 10. The contact angles decreased consistently as the surface was irradiated with UVC light (flux = 9.74×10^{15} photons cm^{-2} s^{-1}). This was attributed to the gradual formation of hydroxylated domains at the surface of the film *via* the photoinduced hydrophilicity (PIH) mechanism. After 120 min of irradiation, the surface was inundated with hydroxyl groups as the water-droplet contact angle was minimized. A 3-dimensional bar chart of water droplet contact angle against cumulative UVC irradiations is shown in Figure 9. A smooth progression to hydrophilicity was observed at each position with cumulative irradiations. After saturating the films with UVC light (120 min), no further decrease in contact angle was observed. A trend in the maximum level of hydrophilicity was revealed, where from position A10 (4.6°) to J10 (18°) a decrease in maximum surface wettability was seen.

The mechanism of PIH has been well established for the rutile phase of TiO_2, where little work on the anatase phase has followed suit.[2] The PIH mechanism requires photoexcitations to function, where the number of active sites on the surface of the material dictates the number of hydroxyl domains that can form. For rutile TiO_2, it was found that the formation of hydroxyl domains was most pronounced on the (110) crystal face, where films with greater orientation in this plane showed greater degrees of photoinduced wetting.[2] It is also worthy of note that the PIH process was found to be independent of film-crystallinity. Given that the energy of our light source (4.88 eV) far surpassed the bandgap energy of all positions tested (Table 2), the degree of photoinduced wetting would have primarily depended on the number of surface active sites. However, a comparison between saturated water droplet contact angle and surface roughness, a measure of surface area, showed a weak linear relationship (r^2 = 0.50). As some facets in rutile TiO_2 show more prominent degrees of photoinduced surface wetting than others, we compared the trend in saturated water droplet contact angles against the degree of preferred orientation in each crystal plane. The strongest relationship was observed upon comparing the degree of preferred orientation in the (211) crystal plane and saturated contact angle (r^2 = 0.81). Given that the primary crystal plane for PIH processes in anatase TiO_2 is, to our knowledge, yet to be identified, these trends highlighted the prominence of the (211) plane.

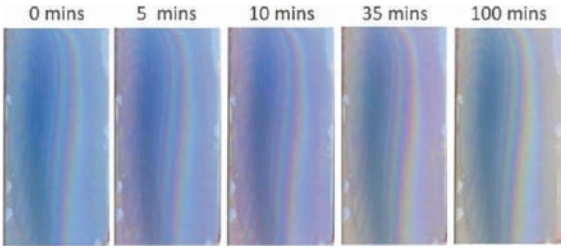

Figure 10. Time line of the photocatalytic reduction of a resazurin-based intelligent ink evenly deposited over the combinatorial film.

Photocatalysis Mapping. The combinatorial film was coated with an even layer of "intelligent ink". The photoreduction reaction was induced by UVA light (flux = 4.69×10^{15} photons cm^{-2} s^{-1}) and monitored solely through digital photography. A time-line of the reaction is shown in Figure 10. Before the reaction was initiated (0 min), the even layer of the royal blue colored ink as well as some blue coloration from the W^{5+} ions was observed. After 5 min of UVA irradiation, the ink had changed color from royal blue to pink solely along the left strip of the combinatorial film. This was due to the photoreduction of the resazurin redox dye (royal blue) to its intermediate resorufin (pink).[36] A transitional change to pink, from left to right, was observed with further irradiations. After 100 min total irradiation, the ink had been fully degraded to its bleached intermediates. The response indicated that the film was increasingly more photocatalytically active from the right side of the film to the left. Such changes in digital color were recently shown to be directly related to the kinetics of the photoreduction reaction.[25,26] The times at which the red components of digital color plateaued were determined by fitting data to a Boltzmann model. The photoreduction rate (molecules photoreduced cm^{-2} s^{-1}) at each grid position was subsequently determined (Supporting Information; S2). A general trend was observed, whereby the rate of UVA photocatalysis varied more substanstially across rows and less so in columns. For comparison, the UVC (flux = 9.74×10^{15} photons cm^{-2} s^{-1}) photooxidation of a stearic acid overlayer was assessed for positions across row 10. The rates of UVC (stearic acid) and UVA (resazurin intelligent ink) photocatalysis were converted into formal quantum efficiencies (molecules destroyed per incident photon) and compared. A linear correlation with a good degree of fit was observed ($r^2 = 0.82$).

When assessing the trends in photocatalysis across a number of samples, one must account for variations in thickness, bandgap energy, crystallinity, surface roughness, and impurity dopant level, as the activity of a photocatalyst is dependent on these physical properties. The thickness and bandgap energy of a semiconductor will determine the number of UVA photons the material will absorb. The formal quantum yield (FQY) accounts for the number of photons absorbed. Any change in thickness or bandgap energy can therefore be discounted when comparing FQYs. In trying to account for the decreasing trend in FQY across row 10 from position A10 to J10, the average crystallite size, surface roughness, and tungsten doping level were separately compared against this measure of photocatalysis. A weak relationship was observed between surface roughness and FQY ($r^2 = 0.66$). This indicated that the number of active surface sites to reduce the redox dye was not the primary cause for the variations observed. A strong linear correlation between impurity dopant level and decreasing FQY was observed ($r^2 = 0.81$) and an even stronger degree of correlation between average crystallite size and FQY ($r^2 = 0.92$). This indicated two possible pathways for the detriment to photocatalysis:

(i) an increased presence of tungsten centers induced the recombination of photoexcited electrons and holes and/or
(ii) an increased presence of tungsten impurities disrupted the anatase TiO_2 lattice, decreasing film-crystallinity and photoexcited electron and hole movement.

As the degree of film-crystallinity was primarily dictated by the level of tungsten doping in this system, the relationship between tungsten doping level and photocatalysis was a remnant of this relationship.

Previous studies on enhancing the photocatalytic activity of anatase TiO_2 through tungsten doping have entailed the formation of WO_3-TiO_2 composites consisting of WO_3 grains within a TiO_2 host matrix *via* some sol−gel synthesis.[9,32] Significant enhancements in the activity of these composite systems were observed, where dopant levels between 2 and 3 atom % were optimal.[9,30,32] This increase in activity was explained through a charge separation model where WO_3 sites could transfer photoexcited holes into the valence band of the TiO_2 matrix and TiO_2 could transfer photoexcited electrons into the conduction band of WO_3, hindering recombination and driving photocatalytic processes.[9] However, in this combinatorial study, tungsten entered anatase TiO_2 as a solid solution and was incapable of such functionality. This was reflected in the photocatalytic activity of our material, where the most active position (A10) showed a lower FQE of 5.21×10^{-5} (stearic acid molecules degraded/incident photon) compared with an optimized 2 atom % WO_3-TiO_2 sol−gel composite with a FQE of 7.72×10^{-5}.[11]

Conductivity Mapping. The benefits of doping anatase TiO_2 thin-films for future use in photovoltaic devices or as transparent conducting oxide (TCO) protective layers are clear given their durability to humidity or acid degradation[58] and hydrogen radical exposure[59,60] compared with traditional SnO_2 and ZnO_2 based TCOs. However, tuning the dopant level precisely to achieve optimized electrical resistances is a venture of large commercial importance. The electrical sheet resistance ($\Omega/\square$) was determined using the van der Pauw method.[38] The sheet resistance differed by several orders of magnitude across the film. The expected trend was observed, whereby increased conductivity was observed with film thickness. The resistance along columns I and J exceeded the detection limits of the apparatus, so the sheet resistance was not determined. A 3-dimensional contour map of the $\log_{10}$(sheet resistance ($\Omega/\square$)) for all other columns is supplied in the Supporting Information (S3). The sheet resistances were converted into resistivities and showed a uniform increase from columns A to H (Table 2).

In a previous study of W^{5+} doped anatase TiO_2 single crystals, it was shown through computation and experiment that increased doping increased the number of charge carriers.[28] However, upon comparing our tungsten doping levels with resistivity, a reverse trend was observed where increased tungsten doping increased resistance. The resistivity of an n-doped semiconductor such as tungsten doped anatase TiO_2 is dependent upon two primary factors:

(i) the charge carrier concentration (n) and
(ii) the mobility of charge carriers (μ).

By introducing small levels of tungsten into the anatase TiO_2 framework at position A10, film-resistivity decreased relative to that of pure anatase TiO_2 by several orders of magnitude (10^5 Ω m).[61] This was attributed to the introduction of charge carriers into the

system with little disruption to the lattice. The increased level of tungsten doping seen across row 10 should have increased the number of charge carriers; however, an increase in resistance was observed. Therefore, the mobility of these charge carriers (μ) must have been impeded to counter this increase in charge carrier concentration (n). From XRD experiments, an increase in amorphousness was observed with increased tungsten doping. This disruption of the TiO_2 lattice would have caused a decrease in the mobility of the charge carriers. From the decrease in resistivity seen across the row, it was clear that the detriment to charge carrier mobility was greater than the increase in charge carrier concentration. The most effective balance between these two counteracting properties was found at position A10, where a W-doping level of 0.42 atom % was present. A strong linear relationship between the underlying film crystallinity and resistivity was observed ($r^2 = 0.85$). This correlated with what had previously been observed in the literature for niobium doped anatase TiO_2,[17,62,63] where mobility effects dominate. The combinatorial W-doped anatase TiO_2 system investigated here indicated that some optimum level of W-doping for increased film-conductivity lies in the range $0 < W/Ti$ atom % ≤ 0.42. Nevertheless, these films were grown at atmospherics pressure, where it has been found that annealing similar materials under vacuum (3×10^{-3} Pa) at higher temperatures (650 °C) can significantly decrease film-resistivity to levels as low as 1.5×10^{-4} Ω m for dopant levels as high as 6.3 atom %, where such a decrease in film-resistivity is due to an increase in the mobility of the charge carriers through increased oxygen vacancy formation and film-crystallinity.[28]

CONCLUSIONS

A combinatorial thin-film comprised solely of the anatase TiO_2 phase with varying levels of tungsten (primarily W^{5+}) solid solution doping ($0.38 \leq W/Ti$ atom % ≤ 13.8) was formed by the combinatorial APCVD reaction of $TiCl_4$ (Ti source), WCl_6 (W source), and ethyl acetate (O source) at 525 °C. This was the first time in which a thin-film of a W-doped anatase TiO_2 solid solution was formed by a CVD process. By partially mixing the metal sources, a combinatorial film with a compositional profile that varied primarily in the lateral plane was formed. Using high-throughput screening methods, inter-relationships between the physical and functional properties of the system were rapidly established:

(i) A strong linear inter-relationship between the tungsten doping level, unit cell volume, and degree of shift in the principle Raman active E_g vibrational mode was found, which provided a simpler route to estimating the level of tungsten incorporated in anatase TiO_2 solid solutions through either Raman spectroscopy or X-ray diffraction as opposed to wavelength dispersive X-ray analysis. Furthermore, tungsten doping was found to increase the unit cell predominantly in the *ab* plane.

(ii) The UV photocatalytic activity of the film was most dependent on film-crystallinity. Increased W^{5+} doping disrupted the lattice and increased photogenerated electron and hole recombination processes, which lowered the photocatalysis.

(iii) Electrical-resistivity was most dependent on charge transport properties rather than charge carrier concentration, where, under the experimental conditions imposed, the optimum balance between increased charge carrier concentration through W-doping and the detrimental lattice disruptions that follow was at a doping level of ≈0.4 atom %.

(iv) The degree of photoinduced surface wetting was most highly dependent on the level of preferred orientation in the (211) plane, where increased orientation in this plane increased the maximum degree of photoinduced surface wetting. Given that the primary crystal plane for the photoinduced wetting process in anatase TiO_2 is yet to be identified in the literature, this finding highlighted the importance of the (211) plane in the photoinduced hydrophilicity mechanism.

Analyzing combinatorial thin-films synthesized by the cAPCVD route in conjunction with high-throughput screening methods provides a shortcut to identifying physical−functional property inter-relationships and offers a rapid method for discovering optimum compositions and new materials.

ASSOCIATED CONTENT

Supporting Information. Topographical images, photoreduction rate at each grid position, and 3-dimensional contour maps of the $\log_{10}$(sheet resistance (Ω/□)) for all other columns. This material is available free of charge via the Internet at http://pubs.acs.org.

AUTHOR INFORMATION

Corresponding Author
i.p.parkin@ucl.ac.uk

ACKNOWLEDGMENT

I.P.P. wishes to thank the EPSRC for funding and to express gratitude to Professor Andrew Mills (Strathclyde) for the intelligent ink used in photocatalysis studies and to Cardiff University for allowing the use of their XPS instrument.

REFERENCES

(1) Mills, A.; Hunte, S. *J. Photochem. Photobiol., A* **1997**, *108*, 1.
(2) Fujishima, A.; Zhang, X.; Tryk, D. *Surf. Sci. Rep.* **2008**, *63*, 515.
(3) Selli, E.; Chiarello, G. L.; Quartarone, E.; Mustarelli, P.; Rossetti, I.; Forni, L. *Chem. Commun.* **2007**, *1*, 5022.
(4) Mills, A.; Valenzuela, M. *J. Photochem. Photobiol., A* **2004**, *165*, 25.
(5) Osterloh, F. E. *Chem. Mater.* **2008**, *20*, 35.
(6) Savage, N. *Sens. Actuators, B* **2001**, *79*, 17.
(7) Dunnill, C. W.; Aiken, Z. A.; Pratten, J.; Wilson, M.; Morgan, D. J.; Parkin, I. P. *J. Photochem. Photobiol., A* **2009**, *207*, 244.
(8) Page, K.; Palgrave, R. G.; Parkin, I. P.; Wilson, M.; Savin, S. L. P.; Chadwick, A. V. *J. Mater. Chem.* **2007**, *17*, 95.
(9) Rampaul, A.; Parkin, I. P.; O'Neill, S. A.; Desouza, J.; Mills, A.; Elliott, N. *Polyhedron* **2003**, *22*, 35.
(10) Dunnill, C. W.; Aiken, Z. A.; Kafizas, A.; Pratten, J.; Wilson, M.; Morgan, D. J.; Parkin, I. P. *J. Mater. Chem.* **2009**, *19*, 8747.
(11) Kafizas, A.; Kellici, S.; Darr, J. A.; Parkin, I. P. *J. Photochem. Photobiol., A* **2009**, *204*, 183.
(12) Yang, J. Y.; Li, W. S.; Li, H.; Sun, Y.; Dou, R. F.; Xiong, C. M.; He, L.; Nie, J. C. *Appl. Phys. Lett.* **2009**, *95*, 213105.
(13) Beg, S.; Varshney, P. *J. Mater. Sci.* **2007**, *42*, 6274.
(14) Karthik, K.; Pandian, S. K.; Jaya, N. V. *Appl. Surf. Sci.* **2010**, *256*, 6829.
(15) Mills, A.; Lepre, A.; Elliott, N.; Bhopal, S.; Parkin, I. P.; O'Neill, S. A. *J. Photochem. Photobiol., A* **2003**, *160*, 213.

(16) O'Neill, S. A.; Clark, R. J. H.; Parkin, I. P.; Elliott, N.; Mills, A. *Chem. Mater.* **2003**, *15*, 46.
(17) Kafizas, A.; Dunnill, C. W.; Parkin, I. P. *J. Mater. Chem.* **2010**, *20*, 8336.
(18) Kafizas, A.; Dunnill, C. W.; Hyett, G.; Parkin, I. P. *ECS Trans.* **2010**, *25*, 139.
(19) Hyett, G.; Green, M.; Parkin, I. P. *J. Am. Chem. Soc.* **2006**, *128*, 12147.
(20) Kafizas, A.; Crick, C.; Parkin, I. P. *J. Photochem. Photobiol., A* **2010**, *216*, 156.
(21) Kafizas, A.; Parkin, I. P. *J. Mater. Chem.* **2010**, *20*, 2157.
(22) Hyett, G.; Parkin, I. P. *Surf. Coat. Technol.* **2007**, *201*, 8966.
(23) Kafizas, A.; Hyett, G.; Parkin, I. P. *J. Mater. Chem.* **2009**, *19*, 1399.
(24) Hyett, G.; Green, M.; Parkin, I. P. *J. Am. Chem. Soc.* **2007**, *129*, 15541.
(25) Kafizas, A.; Mills, A.; Parkin, I. P. *Anal. Chim. Acta* **2010**, *663*, 69.
(26) Kafizas, A.; Adriaens, D.; Mills, A.; Parkin, I. P. *Phys. Chem. Chem. Phys.* **2009**, *11*, 8367.
(27) Takeuchi, U.; Chikamatsu, A.; Hitosugi, T.; Kumigashira, H.; Oshima, M.; Hirose, Y.; Shimada, T.; Hasegawa, T. *J. Appl. Phys.* **2010**, *107*, 023705.
(28) Chen, D.; Xu, G.; Miao, L.; Chen, L.; Nakao, S.; Jin, P. *J. Appl. Phys.* **2010**, *107*, 063707.
(29) Garzella, C. *Sens. Actuators, B* **2003**, *93*, 495.
(30) Lee, Y. C.; Hong, Y. P.; Lee, H. Y.; Kim, H.; Jung, Y. J.; Ko, K. H.; Jung, H. S.; Hong, K. S. *J. Colloid Interface Sci.* **2003**, *267*, 127.
(31) Kafizas, A.; Kellici, S.; Darr, J. A.; Parkin, I. P. *J. Photochem. Photobiol., A* **2009**, *204*, 183.
(32) Li, X. Z.; Li, F. B.; Yang, C. L.; Ge, W. K. *J. Photochem. Photobiol., A* **2001**, *141*, 209.
(33) Casa Software Ltd. http://www.casaxps.com/.
(34) Briggs, D.; Seah, M. P. *Practical Surface Analysis*, 2nd ed.; John Wiley and Sons: Chichester, 1993; p 635.
(35) First Ten Angstroms. http://www.firsttenangstroms.com/.
(36) Mills, A.; Wang, J.; Lee, S.-K.; Simonsen, M. *Chem. Commun.* **2005**, *21*, 2721.
(37) RGB Extractor. http://www.ucl.ac.uk/chemistry/staff/academic_pages/ivan_parkin/research.
(38) van der Pauw, L. J. *Philips Res. Rep.* **1958**, *13*, 1.
(39) Slink, W. E.; DeGroot, P. B. *J. Catal.* **1981**, *68*, 423.
(40) Ashraf, S.; Binions, R.; Blackman, C. S.; Parkin, I. P. *Polyhedron* **2007**, *26*, 1493.
(41) Bathe, S.; Patil, P. *Solid State Ionics* **2008**, *179*, 314.
(42) McGuire, G. E.; Schweitzer, G. K.; Carlson, T. *Inorg. Chem.* **1973**, *12*, 2450.
(43) Occhiuzzi, M.; Cordischi, D.; Gazzoli, D.; Valigi, M.; Heydorn, P. C. *Appl. Catal., A* **2004**, *269*, 169.
(44) Sarma, D.; Rao, C. *J. Electron Spectrosc. Relat. Phenom.* **1980**, *20*, 25.
(45) Schiavello, M. *J. Solid State Chem.* **1977**, *72*, 67–72.
(46) Ohsaka, T.; Izumi, F.; Fujiki, Y. *J. Raman Spectrosc.* **1978**, *7*, 321.
(47) Wu, K.-R.; Hung, C.-H. *Appl. Surf. Sci.* **2009**, *256*, 1595.
(48) Harunsani, M. H.; Oropeza, F. E.; Palgrave, R. G.; Egdell, R. G. *Chem. Mater.* **2010**, *22*, 1551.
(49) Kim, D.-S.; Yang, J.-H.; Balaji, S.; Cho, H.-J.; Kim, M.-K.; Kang, D.-U.; Djaoued, Y.; Kwon, Y.-U. *CrystEngComm* **2009**, *11*, 1621.
(50) Patterson, A. *Phys. Rev.* **1939**, *56*, 978.
(51) Toby, B. H. *J. Appl. Crystallogr.* **2001**, *34*, 210.
(52) Chan, T. S.; Lee, J.-F.; Liu, R. S. *J. Phys.: Conf. Ser.* **2009**, *190*, 012095.
(53) Carvajal, J. J.; Solé, R.; Gavaldà, J.; Massons, J.; Díaz, F.; Aguiló, M. *Chem. Mater.* **2003**, *15*, 2730.
(54) Swanepoel, R. J. *J. Phys. E: Sci. Instrum.* **1983**, *16*, 1214.
(55) Evans, P.; Pemble, M. E.; Sheel, D. W. *Chem. Mater.* **2006**, *18*, 5750.
(56) Tauc, J. *Mater. Res. Bull.* **1968**, *3*, 37.
(57) Moss, T. S. *Proc. Phys. Soc.: B* **1954**, *67*, 775.
(58) Neumann, B.; Bierau, F.; Johnson, B.; Kaufmann, C. A.; Ellmer, K.; Tributsch, H. *Phys. Status Solidi (B)* **2008**, *245*, 1849.
(59) Kambe, M.; Sato, K.; Kobayashi, D.; Kurokawa, Y.; Miyajima, S.; Fukawa, M.; Taneda, N.; Yamada, A.; Konagai, M. *Jpn. J. Appl. Phys.* **2006**, *45*, L291.
(60) Natsuhara, H.; Matsumoto, K.; Yoshida, N.; Itoh, T.; Nonomura, S.; Fukawa, M.; Sato, K. *Sol. Energy Mater. Sol. Cells* **2006**, *90*, 2867.
(61) Tang, H.; Prasad, K.; Sanjinés, R.; Lévy, F. *Sens. Actuators, B* **1995**, *26*, 71.
(62) Sheppard, L. R.; Bak, T.; Nowotny, J. *J. Phys. Chem. C* **2008**, *112*, 611.
(63) Zhang, S. X.; Dhar, S.; Yu, W.; Xu, H.; Ogale, S. B.; Venkatesan, T. *Appl. Phys. Lett.* **2007**, *91*, 112113.